Supporting Information

Mechanistic understanding of cetyltrimethylammonium bromide-assisted durable $CH_3NH_3PbI_3$ film for stable ZnO-based perovskite solar cells

Yan Guo[a], Xin Li[a,], Leilei Kang[b,]*, Chuanqi Cheng[c], Xiong He[a], Xin Liu[a], Jingyan Liu[a], Yuanchao Li[a], Cunku Dong[c,]**

[a] MIIT Key Laboratory of Critical Materials Technology for New Energy Conversion and Storage, School of Chemistry and Chemical Engineering, State Key Lab of Urban Water Resource and Environment, Harbin Institute of Technology, Harbin 150090, China.

[b] Dalian Institute of Chemical Physics, Chinese Academy of Sciences, Dalian 116023, China.

[c] Institute of New Energy Materials, School of Materials Science and Engineering, Tianjin University, Tianjin 300072, China.

E-mail Address: lixin@hit.edu.cn; leikang@dicp.ac.cn. ; ckdong@tju.edu.cn

1 Experimental section

Materials. Cetyltrimethylammonium bromide ($C_{19}H_{42}NBr$, CTABr, 99 %) was purchased from Sigma-Aldrich. Zinc acetate dihydrate ($Zn(CH_3COO)_2{\cdot}2H_2O$, 99.995 %) and potassium hydroxide (KOH, 95 %) were obtained from Aladdin. 4-tert-butypyridine and lithium bis(trifluoromethanesulfonyl)imide (Li-TFSI, 99.9 %) were acquired from Kanto. Lead iodide (PbI_2, 99.99 %), methylammonium iodide (CH_3NH_3I, > 99.5 %) and 2, 2′, 7, 7′-tetrakis-(N, N-di-4-methoxyphenylamino)-9, 9′ spirobifluorene (Spiro-OMeTAD, 99.8 %) were purchased from Xi'an Polymer Light Technology Corp. Other anhydrous solvent were purchased from J&K Chemical. Where all reagents were used as received without any further purifcation.

Preparation of ZnO nanoparticles. The ZnO nanoparticles (NPs) were synthesized following a procedure described in our previous work [1]. In a typical procedure, 2.36 g $Zn(CH_3COO)_2{\cdot}2H_2O$ was first dissolved in 100 mL of methanol solution. Then, 52 mL of KOH methanol solution (354 mM) was added dropwise into the aforementioned solution. Subsequently, the mixture was kept at 65 °C for 2.5 h under magnetic stirring, leading to the production of ZnO NPs. Then, the obtained ZnO NPs were washed with anhydrous methanol for three times to remove residual precursors. Finally, the ZnO NPs were dispersed into a solution of n-butanol-chloroform-methanol (14:1:1 volume ratio) to form a 20 mg/mL ZnO NPs suspension.

Fabrication of ZnO-based Perovskite Solar Cells. All ZnO-based perovskite solar cells (PSCs) were fabricated on FTO glass substrates (1.5 cm × 2.0 cm). FTO substrates were first etched by zinc powder and 6 M HCl, and ultrasonically cleaned successively with detergent, deionized water, acetone, 2-propanol (IPA), ethanol, followed by an UV-ozone treatment for 20 min. After that, the electron transport material was deposited onto the substrate by spin-coating ZnO solution at 500 rpm. for 3 s and 3000 rpm. for 30 s and dried at room temperature for 10 min. This process was repeated two times to obtain a compact ZnO film. Then, the ZnO film was aged 24 h under ambient conditions. The perovskite layer was synthesized by a two-step spin-coating fabrication protocol. The PbI_2 N, N-dimethylformamide (DMF) solution (460 mg /mL) was first spin-coated on the FTO/ZnO film at 3000 rpm. for 30 s and annealed at 70 °C for 10 min. Subsequently, a solution of CH_3NH_3I (MAI) in IPA (50 mg/mL) was spin-coated on the surface of PbI_2 film at 1000 rpm. for 5 s and 3000 rpm. for 30 s and then annealed at 80 °C for 15 min. Afterward, the CTABr solution dissolved in IPA (2 mM, 5 mM, 10 mM and 20 mM) was spin-coated on the FTO/ZnO/$CH_3NH_3PbI_3$ ($MAPbI_3$) film at 1000 rpm. for 5 s and 3000 rpm. for 30 s, followed by an annealing step at 80 °C for 60 min. As a control sample, the same amount of IPA solvent was spin-coated on the FTO/ZnO/$MAPbI_3$ film at the same operation condition. When the FTO/ZnO/$MAPbI_3$/CTABr film was cooled down to the room temperature, the Spiro-OMeTAD hole transfer layer (80 mg of Spiro-OMeTAD, 28.5 μL 4-tert-butypyridine, 17.5 μL Li-TFSI (520 mg of Li-TFSI in 1 mL of acetonitrile) all dissolved in 1 mL chlorobenzene) was deposited on the top of FTO/ZnO/$MAPbI_3$/CTABr film by spin-coating at 4000 rpm. for 30 s. Finally, about 60 nm thick Au counter electrode was deposited on top of Spiro-OMeTAD film via vacuum thermal evaporation at an evaporation rate 1.0 Å/s. The active area of PSCs was confirmed to be 0.12 cm^2 by a non-reflective metal mask. All processes including fabrication, measurement and storage of devices were carried out under ambient conditions. The environmental temperature and relative humidity (RH) for the fabrication process, *J-V* measurement and work stability investigation were about 25 °C and 60 %, respectively. The RH was 60-65 % when studying the long-term environmental stability.

2 Characterizations

Synchrotron-based grazing incidence X-ray diffraction. The synchrotron-based grazing incidence X-ray diffraction (GIXRD) measurements were conducted at the BL14B1 beamline of Shanghai Synchrotron Radiation Facility (SSRF) using X-ray with a wavelength of 0.6887 Å. The two dimensional GIXRD (2D-GIXRD) patterns were acquired by a MarCCD detector mounted vertically at a distance of around 560 mm from the sample with an exposure time of less than 40 sec at a grazing incidence angle of 0.2°. The 2D-GIXRD patterns were analyzed using software Fit 2D and displayed in scattering vector q coordinates with $q = 4\pi\sin\theta/\lambda$, where θ is half of the diffraction angle and λ is the wavelength of incident X-ray. X-ray diffraction (XRD) pattern was used to analyze crystal structure, which was recorded on a Panalytical Empyrean X-ray diffractometer with a Cu Kα radiation (λ = 1.540598 Å) at a scan rate of 2°/min.

Scanning electron microscopy. The surface morphologies of NPs and films as well as the element energy dispersive X-ray (EDX) line scan were analyzed by cold field emission scanning electron microscopy (SEM, Hitachi, SU8000).

High-angle annular dark-field scanning transmission electron microscopy. High-angle annular dark-field scanning transmission electron microscopy (HAADF-STEM) images and high-resolution element EDX mapping were examined by field emission transmission electron microscope (TEM) operating at an accelerating voltage of 200 kV (FEI, Tecnai G^2 F20 S-TWIN). The perovskite sample was prepared by spin-coating the perovskite precursor solution on the TEM grid.

Atomic force scanning probe microscope. Atomic force scanning probe microscope (AFM, Bruber, Dimension Icon) was used to perform AFM high images and scanning Kelvin probe microscope (SKPM) tests.

Raman spectroscopy and photoluminescence. Raman spectra and photoluminescence (PL) mappings were performed on a Renishaw *inVia* confocal micro-Raman spectroscopy system (λ = 633 or 532 nm).

Time-resolved photoluminescence. Time-resolved photoluminescence (TRPL) spectra were collected on DeltaPro system (HORIBA Scientific).

Ultraviolet-visible absorption spectroscopy. Ultraviolet-visible (UV-vis) absorption spectroscopy measurements were conducted on TU1901 spectrometer (Beijing Purkinje General Instrument Co., Ltd). Static water contact angle was tested using a JC2000C1 contact angle instrument.

Photocurrent density-photovoltage curves and conductivity tests. Photocurrent density-photovoltage (*J-V*) curves of PSCs and conductivity tests were measured by a binding unit of electrochemical workstation (VersaSTAT 3, Ametek, USA) and a class ABB solar simulator (model 94021A, Newport, USA), where the cells were illuminated using an AM 1.5G sunlight (100 mW cm^{-2}), and the intensity of light was standardized by a Newport Oriel standard PV reference cell system (model 91150 V). The scan rate was 0.2 V/s. Space-charge-limited current (SCLC) and electrochemical impedance spectra (EIS) were performed using a VersaSTAT 3 electrochemical workstation (Ametek, USA) in the dark condition. The EIS data was fitted by the software of ZView2 according to the equivalent circuit model. Incident photon-to-electron conversion efficiency (IPCE) was recorded by a QTest Station 500D solar cell quantum efficiency measurement system (CROWNTECH, USA) equipped with a 300 W tungsten lamp power source, a QEM11-S 1/8 m monochromator, a Keithley 2000 multimeter and an opaque chamber. Hall data were collected by a Hall 8800 system.

3 Computational method

All density functional theory (DFT) calculations were performed using Vienna Ab initio Simulation Package (VASP). The projector augmented wave (PAW) pseudopotential with the Perdew-Burke-Ernzerhof (PBE) exchange correlation function was utilized. The cutoff energy of the plane waves basis set was 500 eV and a Monkhorst-Pack mesh of 3 × 3 × 1 was used in K-sampling for surface with a 15 Å vacuum layer. All structures were spin polarized and all atoms were fully relaxed with the energy convergence tolerance of 10^{-4} eV per atom, and the final force on each atom was < 0.01 eV $Å^{-1}$.

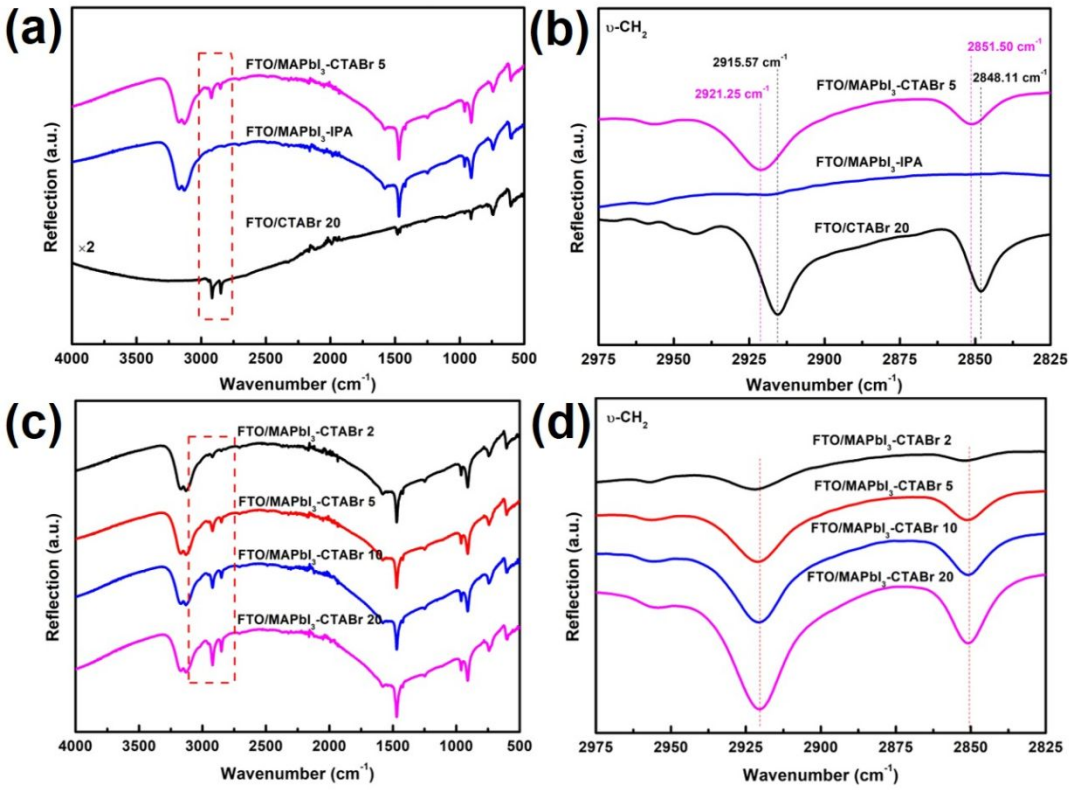

Figure S1. (a) FT-IR spectra and (b) corresponding zoom-in view at the range of 2975-2825 cm^{-1} of FTO/CTABr 20 film, FTO/$MAPbI_3$-IPA film as well as FTO/$MAPbI_3$-CTABr 5 film. (c) FT-IR spectra and (d) corresponding zoom-in view at the range of 2975-2825 cm^{-1} of FTO/$MAPbI_3$ films treated with 2 mM, 5 mM, 10 mM and 20 mM CTABr solution, respectively.

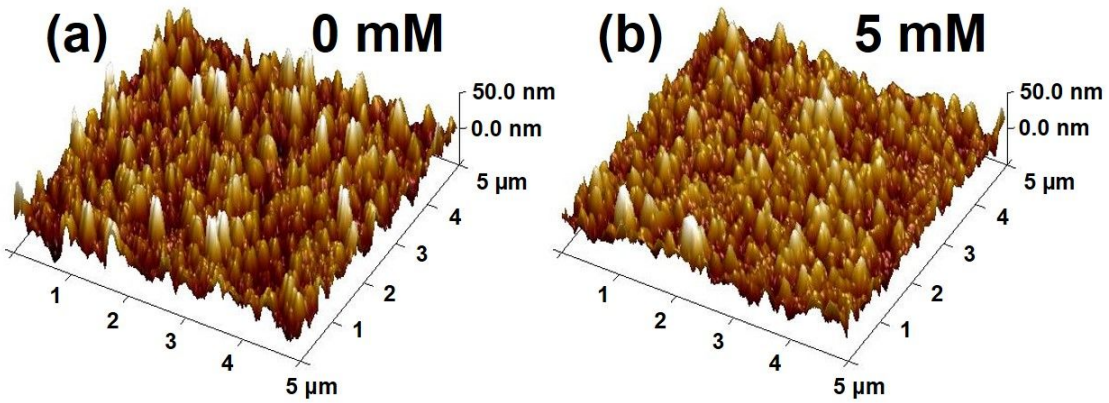

Figure S2. 3D AFM height image of $MAPbI_3$ films treated with (a) 0 mM and (b) 5 mM CTABr solution.

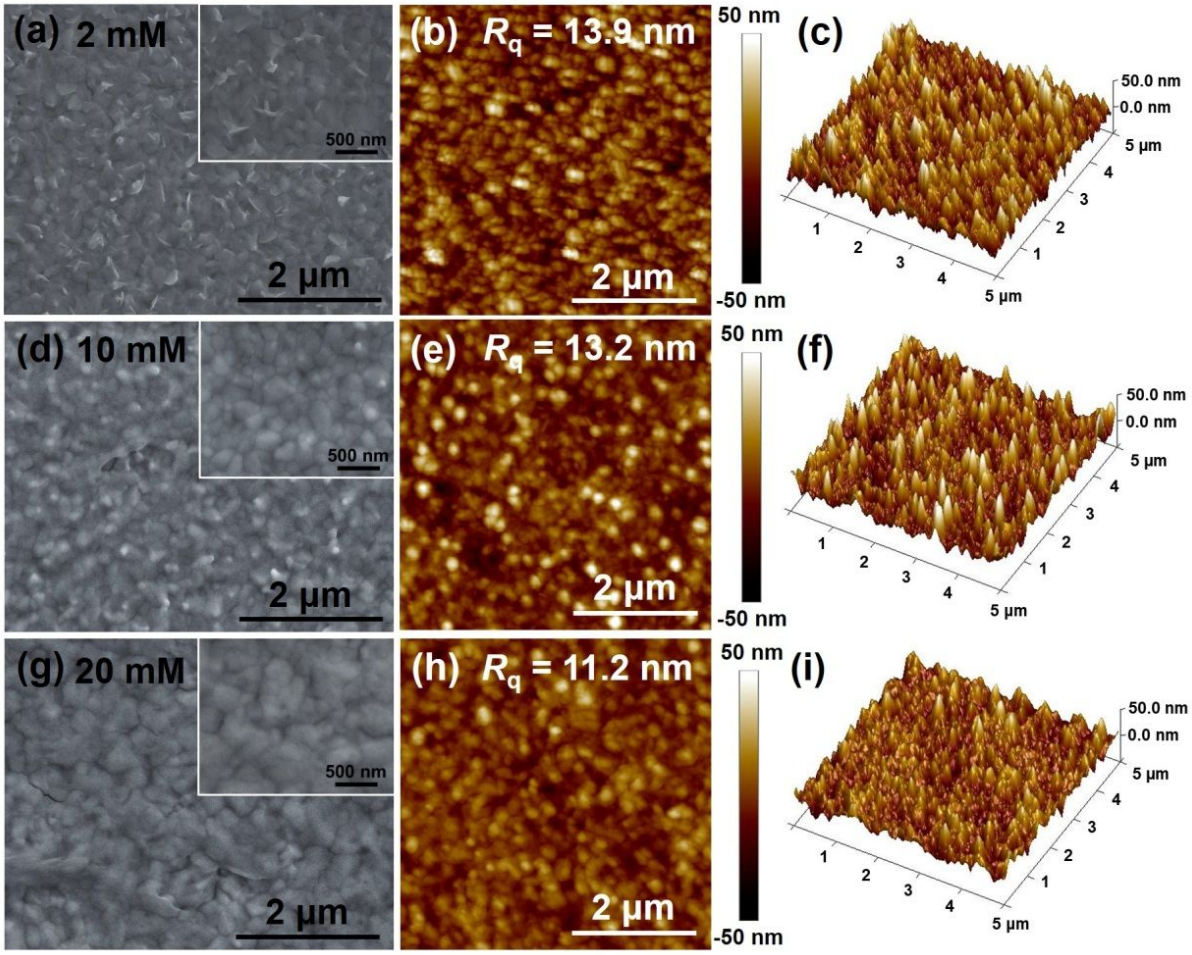

Figure S3. (a) SEM, (b) AFM height and (c) corresponding 3D AFM height images of the $MAPbI_3$ film treated with 2 mM CTABr. (d) SEM, (e) AFM height and (f) corresponding 3D AFM height images of the $MAPbI_3$ film treated with 10 mM CTABr. (g) SEM, (h) AFM height and (i) corresponding 3D AFM height images of the $MAPbI_3$ film treated with 20 mM CTABr.

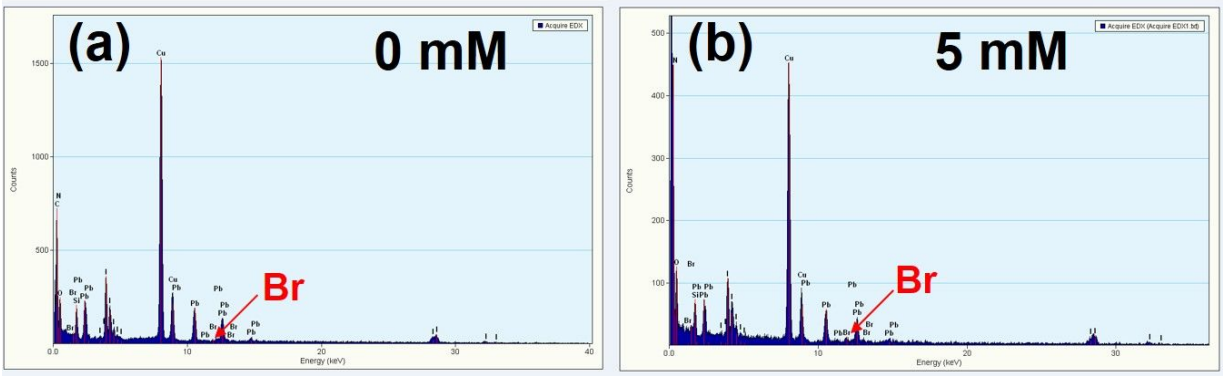

Figure S4. EDX spectra of the (a) $MAPbI_3$-IPA film and (b) $MAPbI_3$-CTABr 5 film.

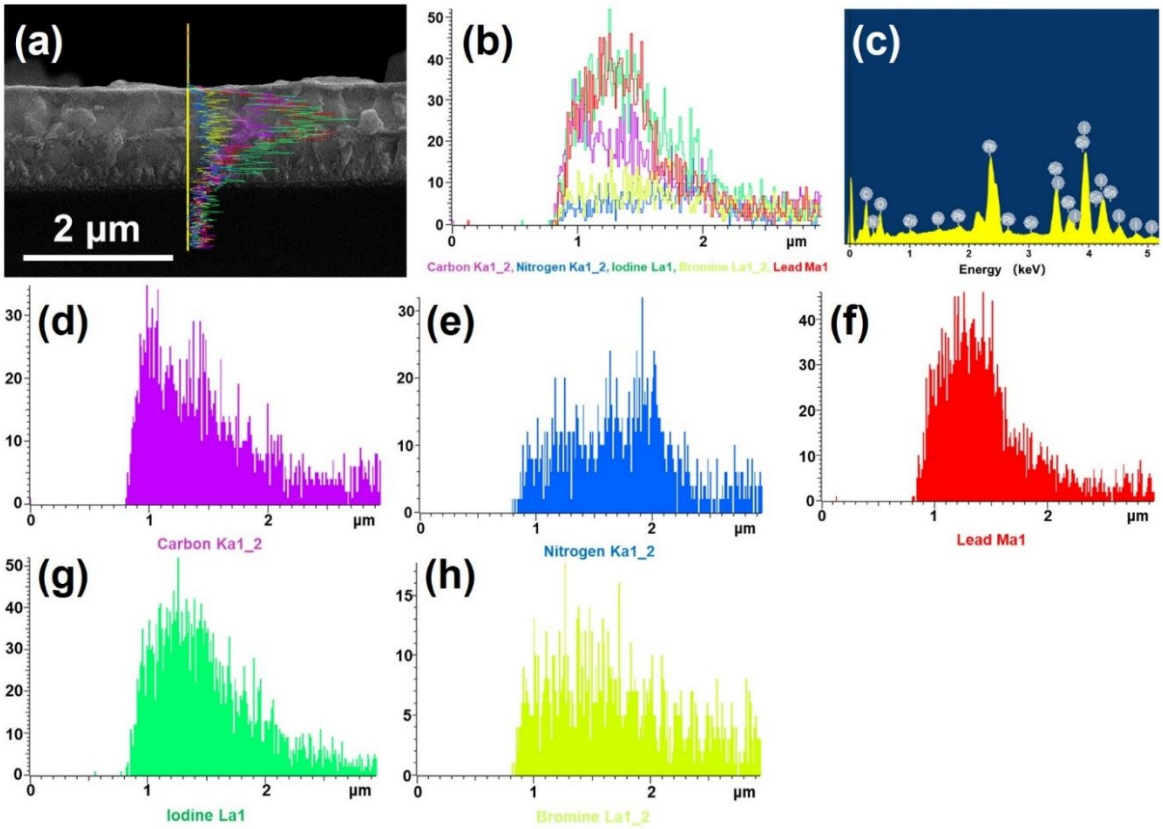

Figure S5. (a) Cross-sectional SEM image of a complete device with the structure of glass/FTO/ZnO/$MAPbI_3$-CTABr 5/Spiro-OMeTAD/Au and (b-h) corresponding distribution information of element of C, N, Pb, I and Br.

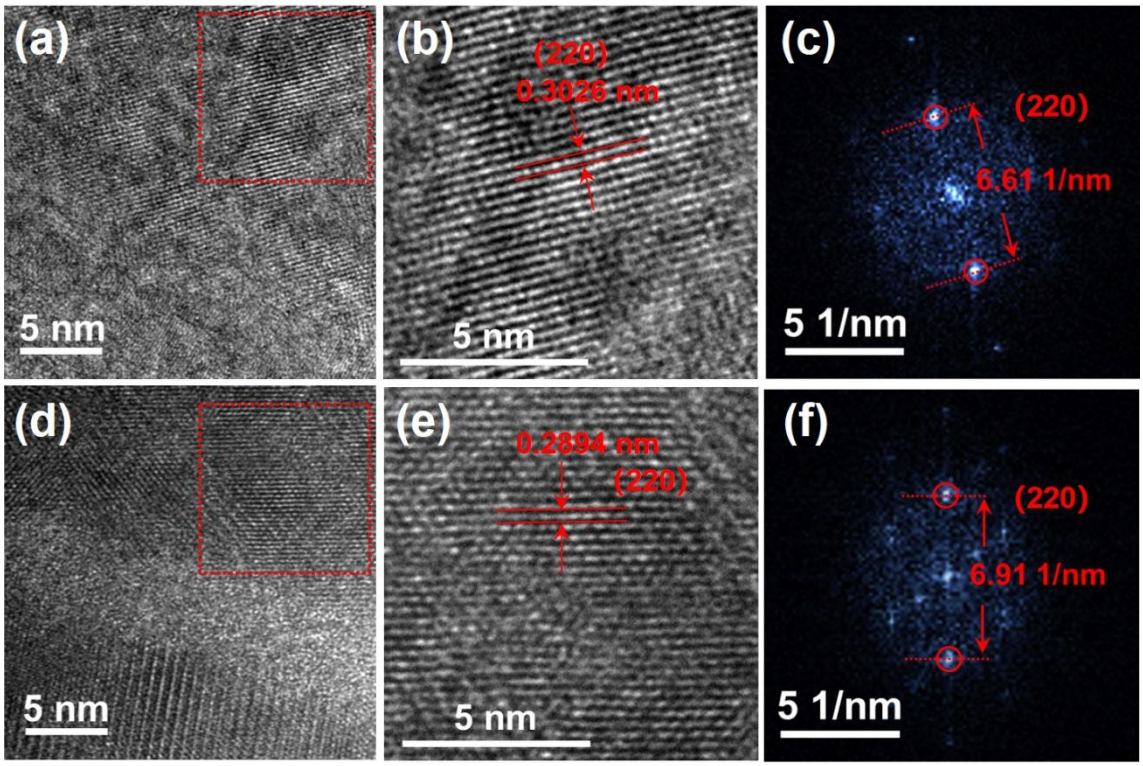

Figure S6. (a) Low and (b) high magnified HR-STEM images as well as (c) corresponding fast Fourier transform (FFT) pattern of $MAPbI_3$-IPA film. (d) Low and (e) high magnified HRSTEM images as well as (f) corresponding fast Fourier transform (FFT) pattern of $MAPbI_3$-CTABr 5 film.

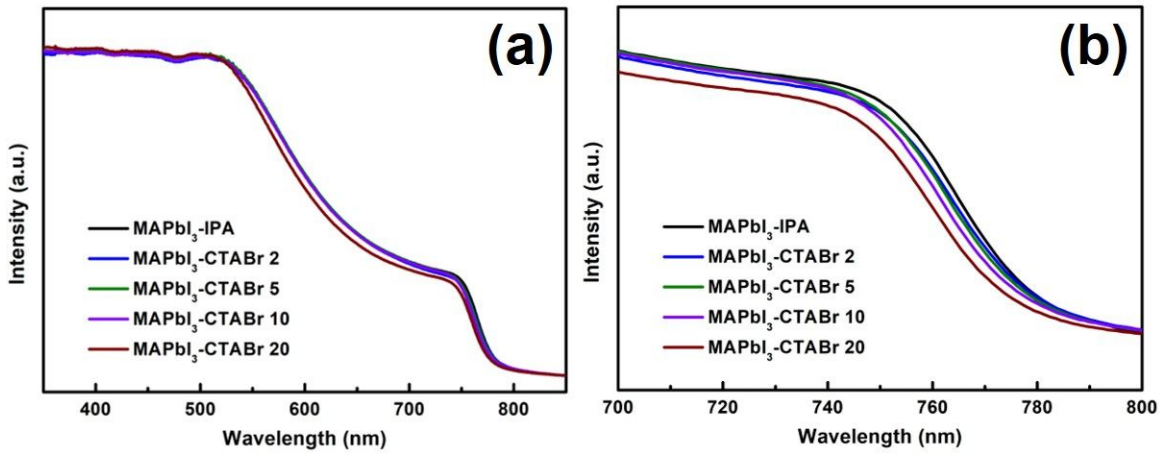

Figure S7. (a) UV-vis spectra and (b) corresponding zoom-in view near the absorption edge of the $MAPbI_3$ films treated with 0 mM, 2 mM, 5 mM, 10 mM and 20 mM CTABr solution, respectively.

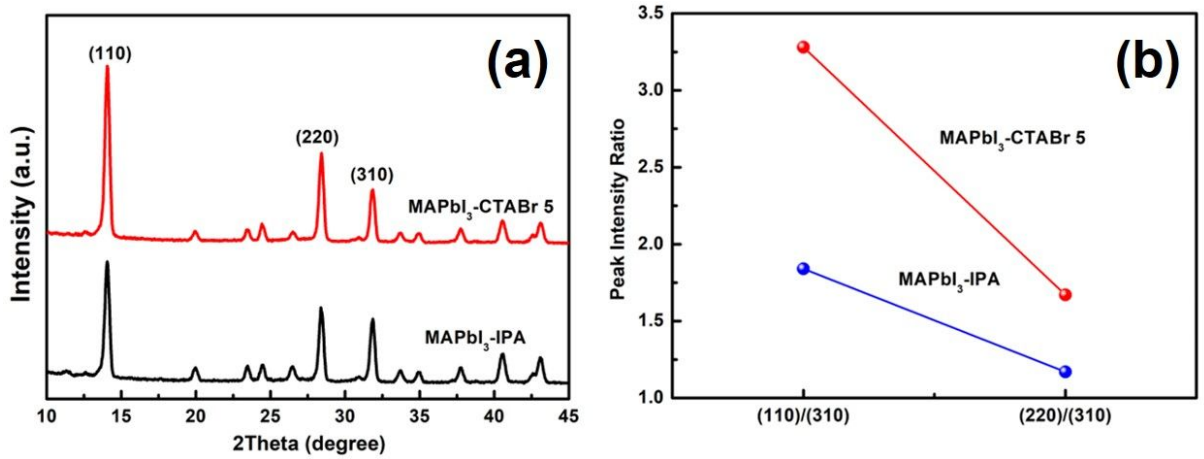

Figure S8. (a) XRD patterns of fresh $MAPbI_3$-IPA film and fresh $MAPbI_3$-CTABr 5 films plotted in Fig. 2e and f. (b) Corresponding peak intensity ratios of (110)/(310) and (220)/(310).

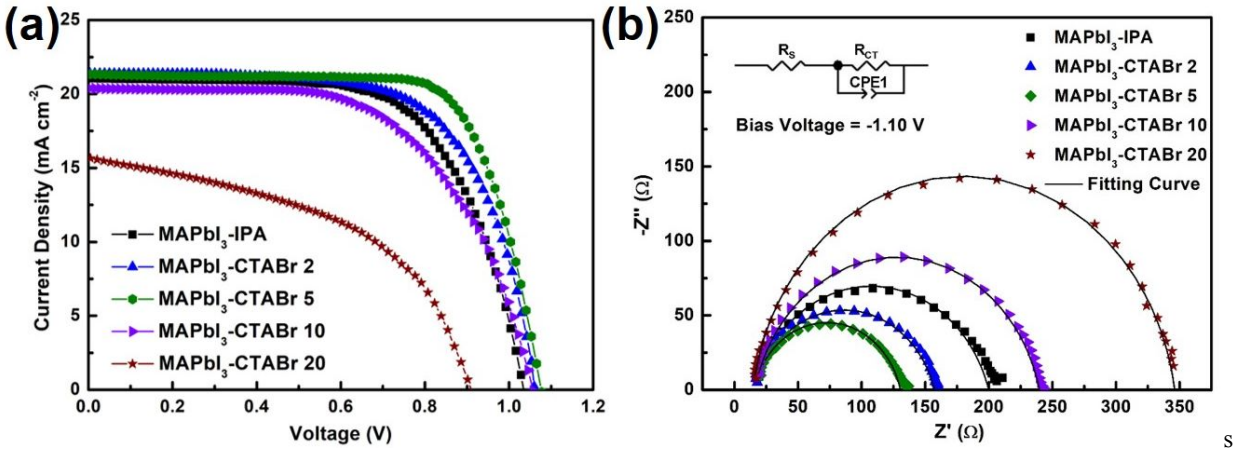

Figure S9. (a) *J-V* curves of PSCs based on $MAPbI_3$-IPA, $MAPbI_3$-CTABr 2, $MAPbI_3$-CTABr 5, $MAPbI_3$-CTABr 10 and $MAPbI_3$-CTABr 20, respectively. (b) Corresponding Nyquist plots of EIS spectra as well as equivalent circuit employed to fit the Nyquist plots measured in dark at the bias voltage of -1.10 V.

Table S1. Detailed *J-V* performance parameters of PSCs based on $MAPbI_3$-IPA, $MAPbI_3$-CTABr 2, $MAPbI_3$-CTABr 5, $MAPbI_3$-CTABr 10 and $MAPbI_3$-CTABr 20, respectively, acquired from Fig. S9a.

Type	J_{SC} (mA cm^{-2})	V_{OC} (V)	FF (%)	PCE (%)
$MAPbI_3$-IPA	21.07	1.036	65.79	14.36
$MAPbI_3$-CTABr 2	21.38	1.061	67.27	15.26
$MAPbI_3$-CTABr 5	21.35	1.076	71.87	16.51
$MAPbI_3$-CTABr 10	20.40	1.057	60.38	13.02
$MAPbI_3$-CTABr 20	16.68	0.911	45.47	6.91

Table S2. Detailed ZView2 fitting parameters of PSCs based on $MAPbI_3$-IPA, $MAPbI_3$-CTABr 2, $MAPbI_3$-CTABr 5, $MAPbI_3$-CTABr 10 and $MAPbI_3$-CTABr 20, respectively, acquired from Fig. S11b.

Type	R_S (Ω)	R_{CT} (Ω)	CPE1-T (F)	CPE1-P (F)
$MAPbI_3$-IPA	15.17	184.40	1.2622 E^{-7}	0.82193
$MAPbI_3$-CTAB 2	15.11	141.81	1.1263 E^{-7}	0.82410
$MAPbI_3$-CTAB 5	15.02	115.37	1.3843 E^{-7}	0.84601
$MAPbI_3$-CTAB 10	16.01	223.71	1.2352 E^{-7}	0.85676
$MAPbI_3$-CTAB 20	16.47	331.62	7.0883 E^{-8}	0.90824

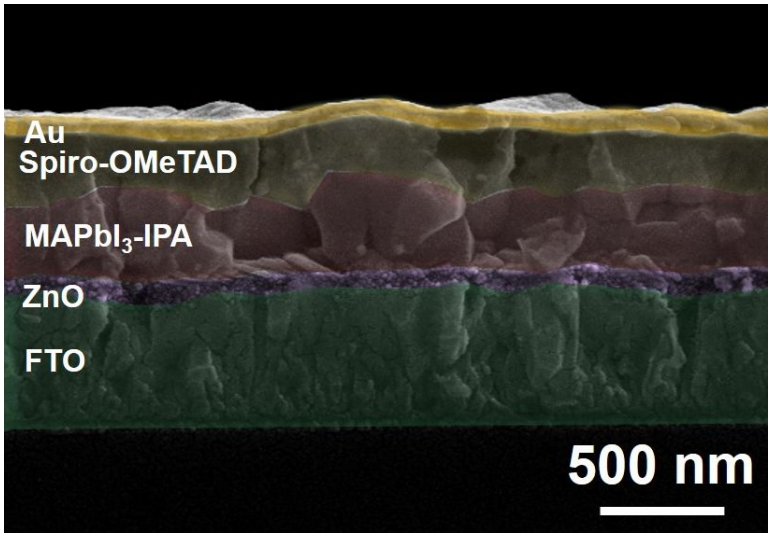

Figure S10. Cross-sectional SEM image of a complete device based on the structure of FTO/ZnO/$MAPbI_3$-IPA/Spiro-OMeTAD/Au.

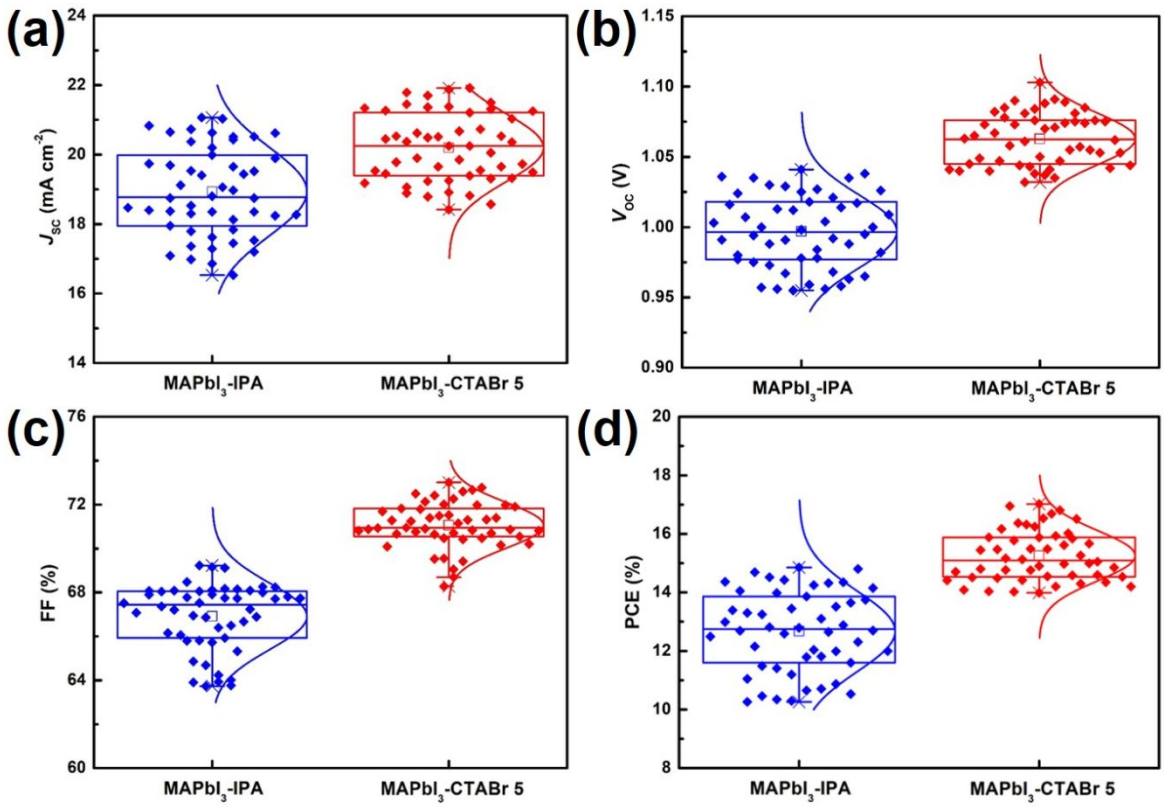

Figure S11. (a) J_{SC}, (b) V_{OC} (c) FF and (d) PCE statistic distribution diagrams of 50 $MAPbI_3$-IPA-based PSCs (blue) and $MAPbI_3$-CTABr 5-based PSCs (red), respectively.

Table S3. Averaged and champion performance parameters of 50 $MAPbI_3$-IPA-based and $MAPbI_3$-CTABr 5-based PSCs as well as corresponding standard deviations.

Type	J_{SC} (mA cm^{-2})	V_{OC} (V)	FF (%)	PCE (%)
$MAPbI_3$-IPA-based PSCs	18.94 ± 1.27	0.997 ± 0.026	66.91 ± 1.52	12.67 ± 1.38
Champion (Reverse and Forward)	20.63 / 20.62	1.041 / 0.990	69.15 / 59.67	14.85 / 12.18
$MAPbI_3$-CTABr 5-based PSCs	20.20 ± 0.98	1.063 ± 0.018	71.06 ± 1.04	15.25 ± 0.87
Champion (Reverse and Forward)	21.87 / 21.80	1.088 / 1.085	71.53 / 66.25	17.02 / 15.67

$$\text{Hysteresis index} = \frac{J_{RS}(0.8V_{OC}) - J_{FS}(0.8V_{OC})}{J_{RS}(0.8V_{OC})} \quad \text{(S1)}$$

Equation S1: $J_{RS}(0.8V_{OC})$ and $J_{FS}(0.8V_{OC})$ represent photocurrent density at 80 % of V_{OC} for the reverse scan (RS) and forward scan (FS), respectively.

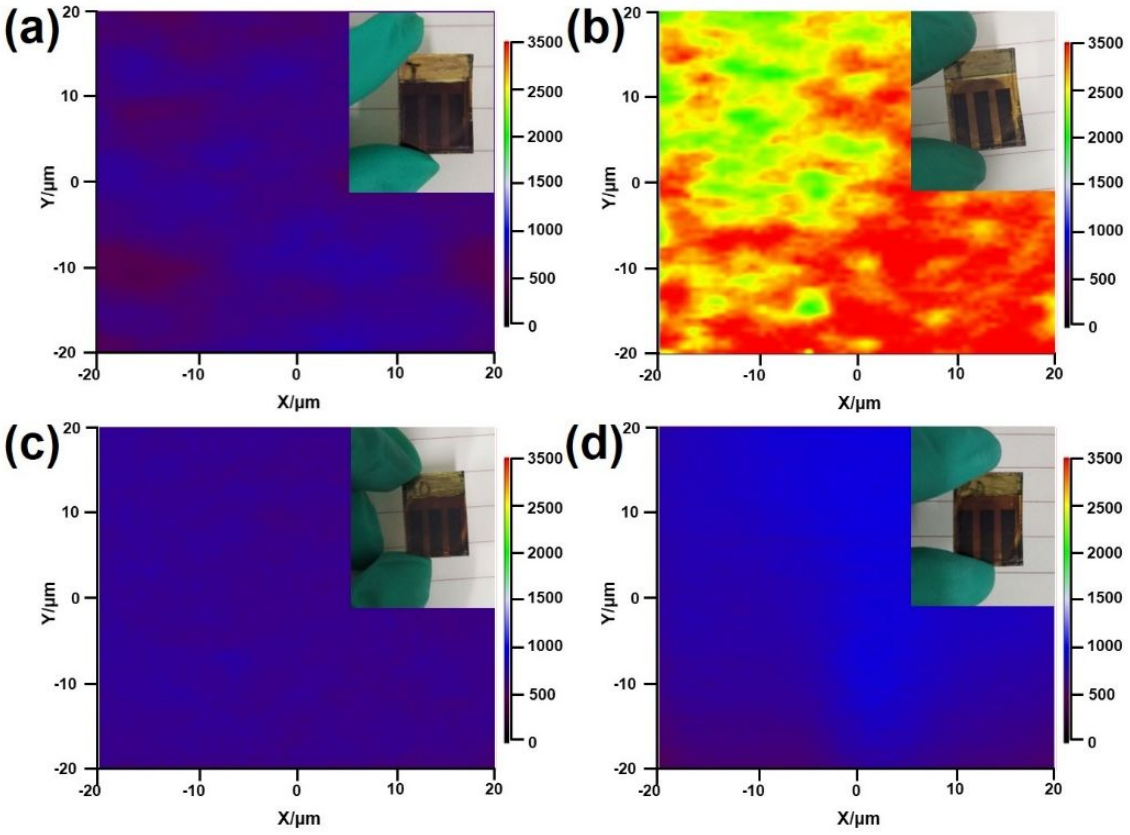

Figure S12. Raman intensity mapping of $MAPbI_3$-IPA-based PSC under MPP and continuous AM1.5G 100 mW cm^{-2} illumination for (a) 0 h and (b) 10 h. Raman intensity mapping of $MAPbI_3$-CTABr 5-based PSC under MPP and continuous AM1.5G 100 mW cm^{-2} illumination for (c) 0 h and (d) 10 h. Insets show the optical images of the corresponding devices. The excitation light source is a 15 mW 532 nm CW laser and the scanning step is 0.5 μm.

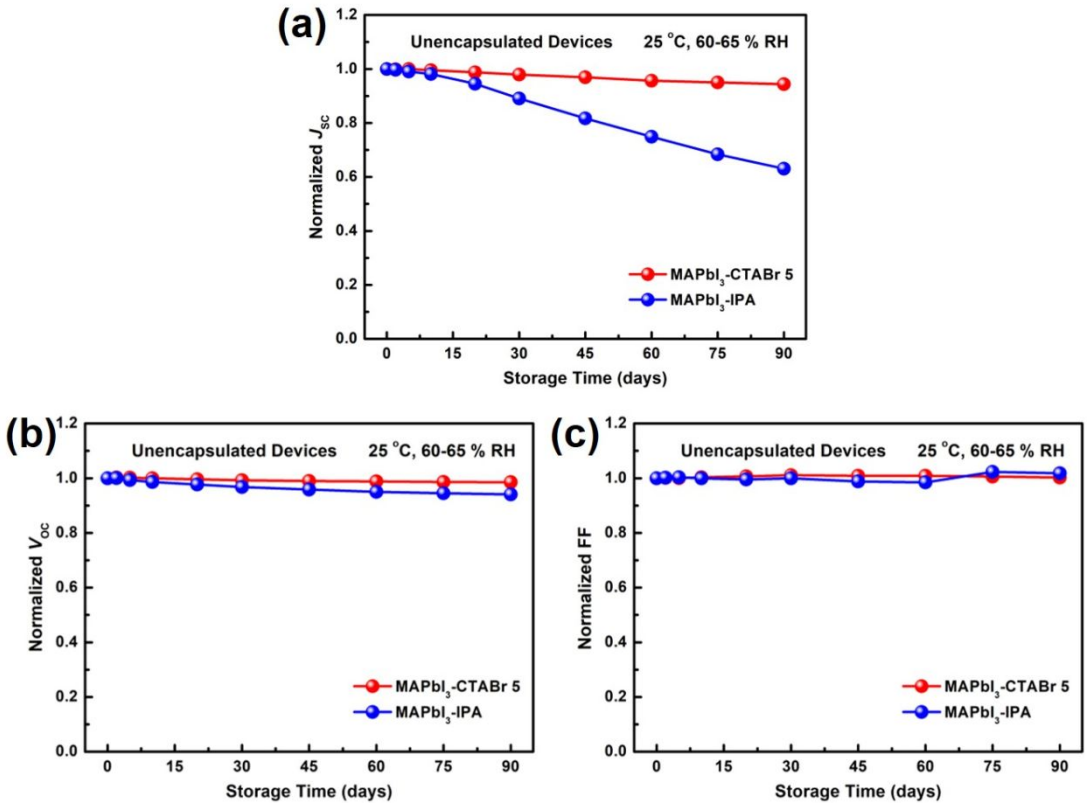

Figure S13. Normalized (a) J_{SC}, (b) V_{OC} and (c) FF evolution of 5 unencapsulated $MAPbI_3$-IPA-based PSC and $MAPbI_3$-CTABr 5-based PSC devices as a function of the storage time, where the devices were kept in air with 60-65 % RH. Insets show the corresponding changes of J_{SC}, V_{OC} and FF with the extension of the storage period.

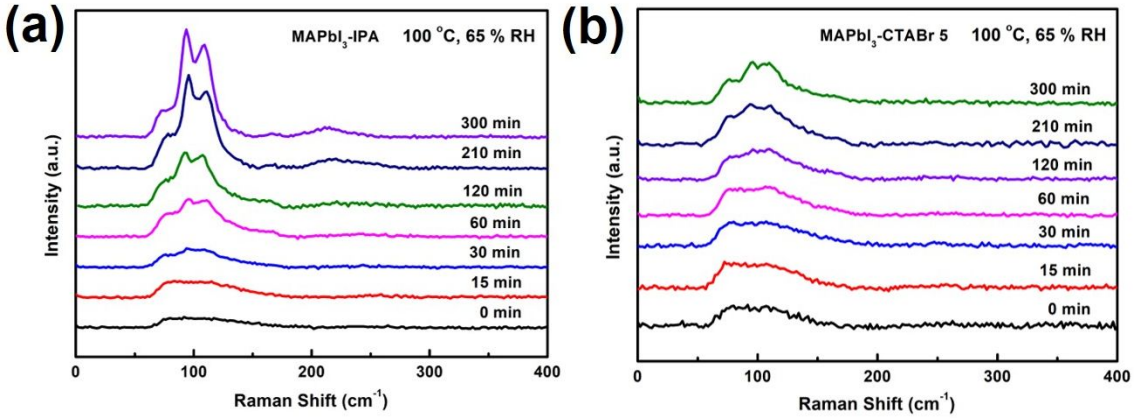

Figure S14. Raman spectra of (a) $MAPbI_3$-IPA and (b) $MAPbI_3$-CTABr 5 film heated at 100 °C and 65 % RH for different time. The excitation light source is a 15 mW 532 nm CW laser.

Table S4. Normalized performance parameters of 5 $MAPbI_3$-IPA-based PSC devices with the extension of storage period.

Storage Time (days)	J_{SC} (mA cm^{-2})/ Normalized J_{SC}	V_{OC} (V)/ Normalized V_{OC}	FF (%)/ Normalized FF	PCE (%)/ Normalized PCE
0	20.37±0.34 / 1.0000	1.0371±0.0038 / 1.0000	69.06±0.75 / 1.0000	14.59±0.25 / 1.0000
2	20.31±0.37 / 0.9971	1.0372±0.0041 / 1.0001	69.17±0.79 / 1.0016	14.57±0.21 / 0.9986
5	20.17±0.46 / 0.9902	1.0303±0.0035 / 0.9934	69.29±0.83 / 1.0033	14.40±0.27 / 0.9870
10	19.99±0.43 / 0.9814	1.0227±0.0035 / 0.9861	69.02±0.79 / 0.9994	14.11±0.29 / 0.9671
20	19.26±0.39 / 0.9455	1.0130±0.0039 / 0.9768	69.73±0.85 / 0.9952	13.41±0.32 / 0.9191
30	18.14±0.38 / 0.8905	1.0035±0.0045 / 0.9676	69.05±0.90 / 0.9999	12.57±0.25 / 0.8616
45	16.64±0.39 / 0.8169	0.9944±0.0039 / 0.9588	68.29±0.93 / 0.9886	11.30±0.26 / 0.7751
60	15.25±0.43 / 0.7487	0.9853±0.0040 / 0.9501	68.02±0.87 / 0.9849	10.22±0.30 / 0.7005
75	13.93±0.37 / 0.6839	0.9803±0.0041 / 0.9452	70.67±0.95 / 1.0233	9.65±0.27 / 0.6614
90	12.84±0.44 / 0.6303	0.9760±0.0045 / 0.9411	70.30±0.91 / 1.0180	8.81±0.33 / 0.6038

Table S5. Normalized performance parameters of 5 $MAPbI_3$-CTABr 5-based PSC devices with the extension of storage period.

Storage Time (days)	J_{SC} (mA cm^{-2})/ Normalized J_{SC}	V_{OC} (V)/ Normalized V_{OC}	FF (%)/ Normalized FF	PCE (%)/ Normalized PCE
0	21.31±0.35 / 1.0000	1.0783±0.0037 / 1.0000	71.24±0.72 / 1.0000	16.37±0.17 / 1.0000
2	21.29±0.29 / 0.9991	1.0811±0.0032 / 1.0026	71.34±0.81 / 1.0014	16.42±0.21 / 1.0031
5	21.30±0.41 / 0.9995	1.0801±0.0035 / 1.0017	71.29±0.85 / 1.0007	16.40±0.19 / 1.0018
10	21.21±0.31 / 0.9953	1.0781±0.0039 / 0.9998	71.46±0.79 / 1.0031	16.34±0.20 / 0.9982
20	21.05±0.33 / 0.9878	1.0745±0.0037 / 0.9965	71.71±0.83 / 1.0066	16.22±0.23 / 0.9908
30	20.87±0.28 / 0.9794	1.0702±0.0041 / 0.9925	71.04±0.81 / 1.0112	16.09±0.25 / 0.9829
45	20.65±0.36 / 0.9690	1.0674±0.0042 / 0.9899	71.86±0.90 / 1.0087	15.84±0.22 / 0.9676
60	20.39±0.29 / 0.9568	1.0655±0.0038 / 0.9881	71.85±0.89 / 1.0086	15.61±0.27 / 0.9536
75	20.24±0.37 / 0.9498	1.0632±0.0045 / 0.9860	71.66±0.87 / 1.0059	15.42±0.25 / 0.9420
90	20.11±0.40 / 0.9437	1.0627±0.0043 / 0.9855	71.41±0.90 / 1.0024	15.26±0.30 / 0.9322

The PL decay fitting curve is based on the biexponential decay function**:**

$$f(t) = A_1\exp(-t/\tau_1) + A_2\exp(-t/\tau_2) + y_0 \quad \text{(S2)}$$

Equation S2:[2] A_1 and A_2 represent the decay amplitude, τ_1 and τ_2 are the lifetime of fast and slow decay phase, and y_0 is a constant for baseline offset.

$$\text{Average decay lifetime } \tau_{avg} = (A_1*\tau_1 + A_2*\tau_2)/(A_1 + A_2) \quad \text{(S3)}$$

Equation S3:[3] A_1 and A_2 represent the decay amplitude, τ_1 and τ_2 are the lifetime of fast and slow decay phase.

Table S6. Fitting parameters based on biexponential decay function for TRPL spectra of $MAPbI_3$-IPA and $MAPbI_3$-CTABr 5 film.

Type	A_1	Fast decay lifetime τ_1 (ns)	A_2	Slow decay lifetime τ_2 (ns)	Average decay lifetime τ_{avg} (ns)
$MAPbI_3$-IPA	0.65	4.28	0.29	47.18	17.52
$MAPbI_3$-CTABr 5	0.47	5.67	0.38	80.78	39.25

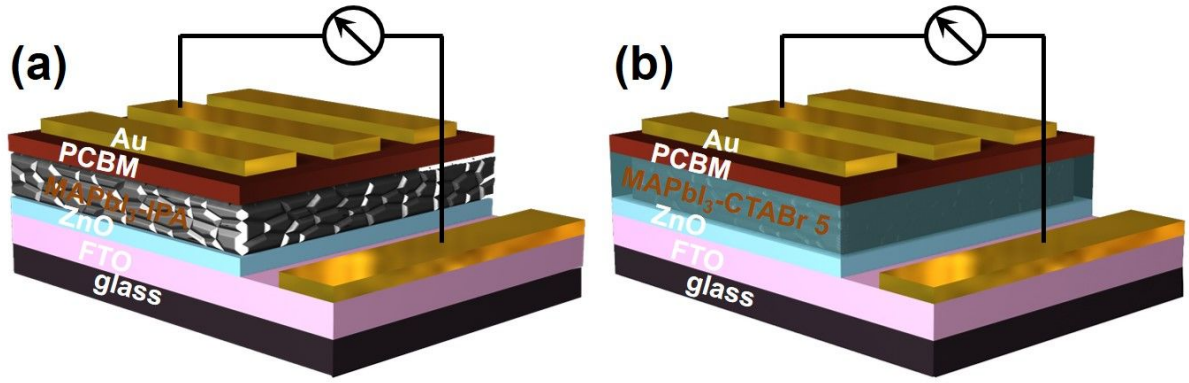

Figure S15. Device structure diagrams for determining (a) $MAPbI_3$-IPA and (b) $MAPbI_3$-CTABr 5 film V_{TFL} point, respectively.

$$n_t = \frac{2\varepsilon\varepsilon_0 V_{TFL}}{eL^2} \quad \text{(S4)}$$

Equation S4: ε is the relative dielectric constant ($\varepsilon = 32$), ε_0 is the vacuum permittivity ($\varepsilon_0 = 8.85 \times 10^{-12}$ F/m), V_{TFL} is the trap-filled limit voltage, e is the elementary charge ($e = 1.6 \times 10^{-19}$ C), and L is the thickness of perovskite films. Here, the thicknesses of the $MAPbI_3$-IPA film and $MAPbI_3$-CTABr 5 film are 371 nm and 388 nm, respectively, which were determined by the step curves acquired from the AFM height images [4-6]. The trap-filled limit region is a range of bias voltage, where all the defects are filled by charge carriers after the V_{TFL} point [6-7]. The first kink point appeared in the dark *I-V* curve is usually considered as the V_{TFL} point.

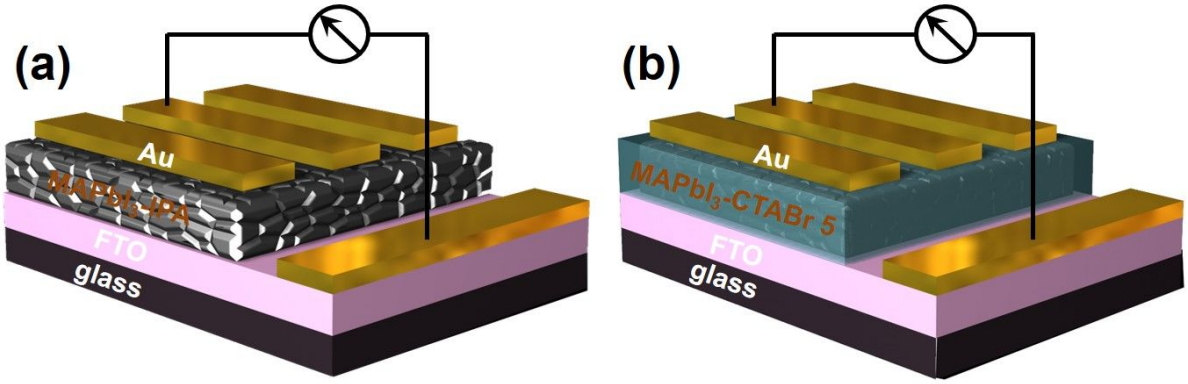

Figure S16. Device structure diagrams for determining (a) $MAPbI_3$-IPA film and (b) $MAPbI_3$-CTABr 5 film conductivity, respectively.

$$\text{Conductivity } \delta = \frac{IL}{US} \quad \text{(S5)}$$

Equation S5: *I, U, L* and *S* represent the current flowing through the perovskite film, the voltage which generates when the current flows through the perovskite film, the thickness and active area of perovskite film, respectively.

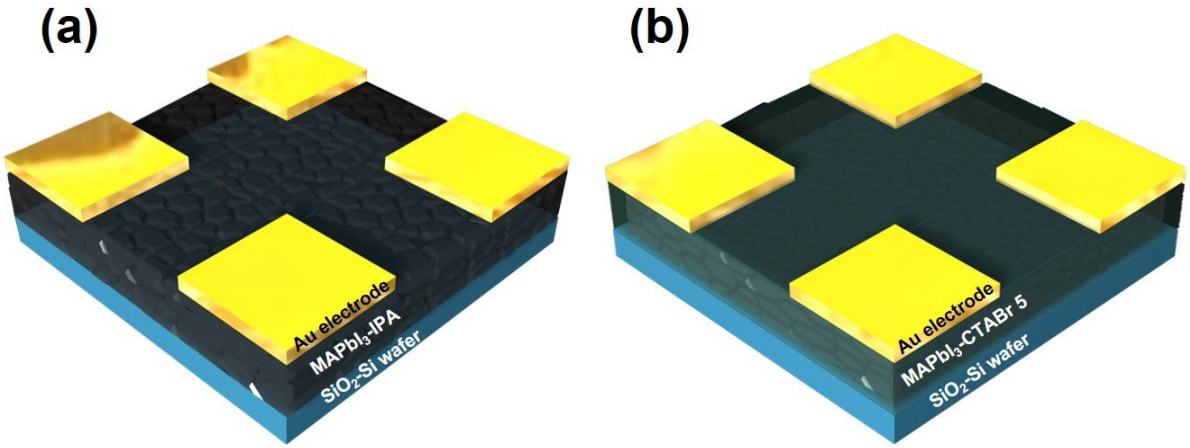

Figure S17. (a) SiO_2-Si wafer/$MAPbI_3$-IPA/Au electrode. (b) SiO_2-Si wafer/$MAPbI_3$-CTABr 5/Au electrode.

$$\delta V_{OC} = n(k_B T/e)\ln(I) + \text{constant} \quad \text{(S6)}$$

Equation S6: n is the ideality factor, k_B is the Boltzmann constant ($k_B = 1.38 \times 10^{-23}$ J/K), e is the elementary charge ($e = 1.6 \times 10^{-19}$ C), T is the absolute temperature ($T = 300$ K), and I is the light intensity [7].

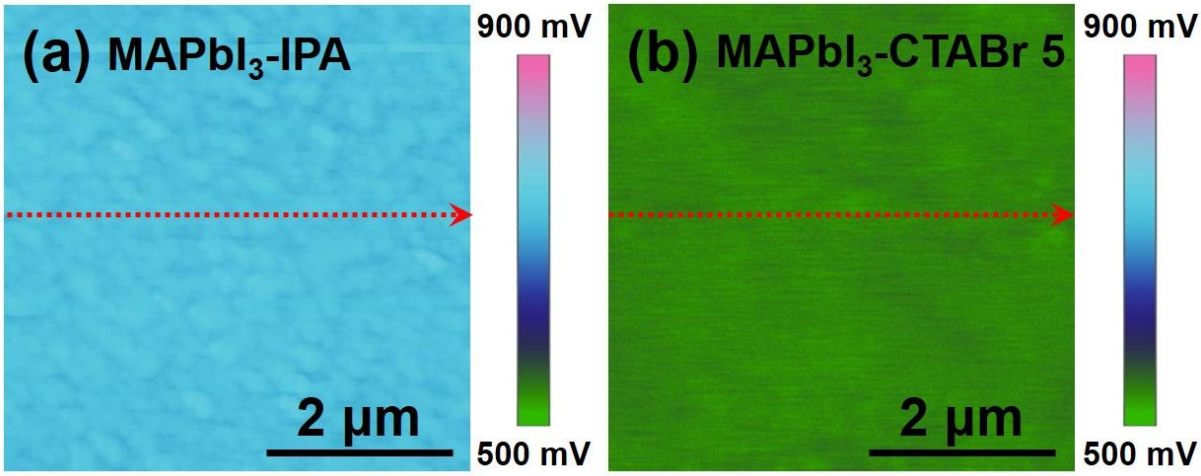

Figure S18. Surface potential images of (a) $MAPbI_3$-IPA film and (b) $MAPbI_3$-CTABr 5 film deposited on FTO substrates.

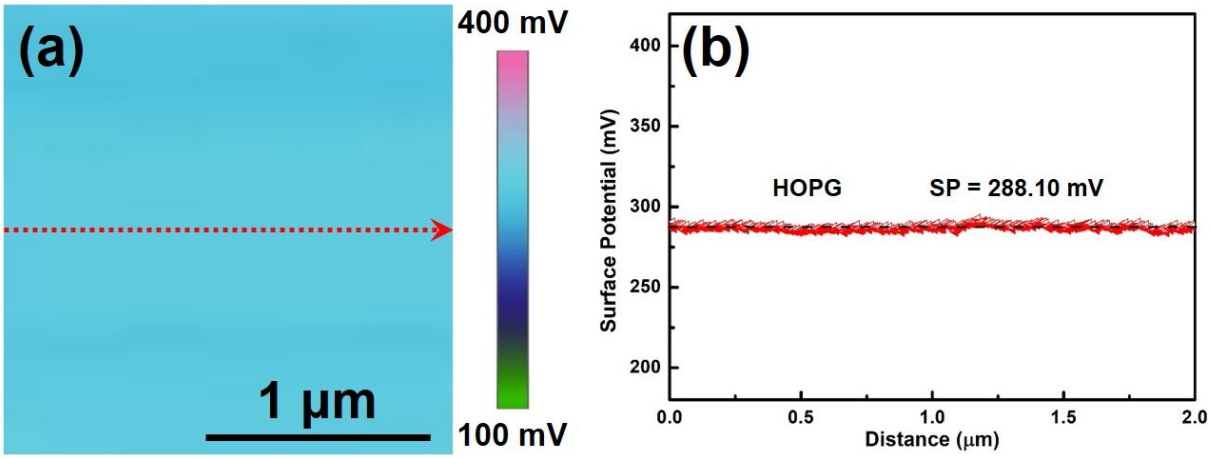

Figure S19. (a) Surface potential images of HOPG. (b) Surface potential (SP) of HOPG obtained from Fig. S23a.

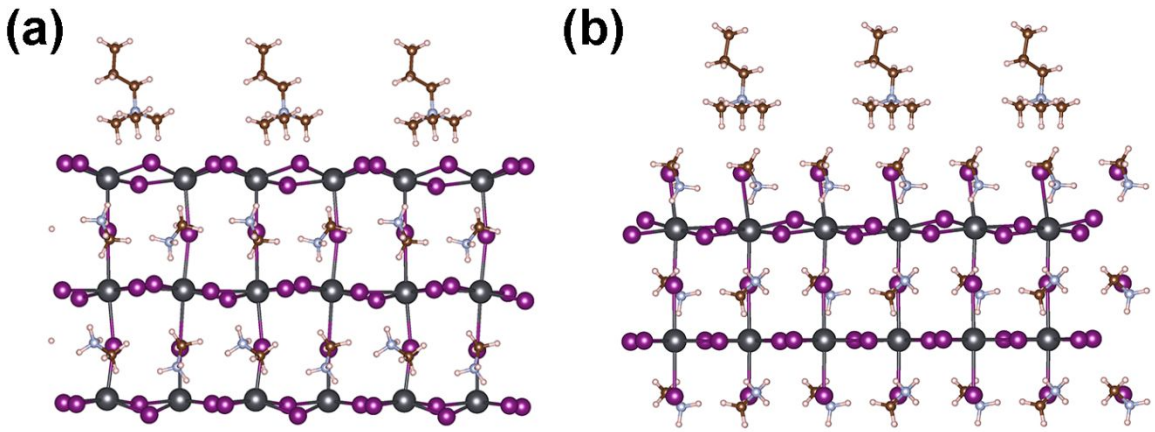

Figure S20. $MAPbI_3$ slab model with CTA^+: (a) PbI_2-rich surface and (b) MAI-rich surface.

Table S7. Surface potentials and work functions of $MAPbI_3$-IPA film and $MAPbI_3$-CTABr 5 film.

Type	$MAPbI_3$-IPA	$MAPbI_3$-CTABr 5	HOPG
Surface Potential (SP, mV)	733.79	560.83	288.10
ΔSP[a]	445.69	272.73	0.00
Work Function[b] (WF, eV)	5.20	5.02	4.75[c]

[a] ΔSP is the surface potential change of sample relative to HOPG. ΔSP=SP (sample) – SP (HOPG);

[b] $WF = WF_0 + e\Delta SP$, where WF_0 is the work function of HOPG (4.75 eV);

[c] HOPG (highly oriented pyrolytic graphite) was used as a reference with the work function of 4.75 eV given by the supplier [8].

References

(1) Guo, Y.; Kang, L.; Zhu, M.; Zhang, Y.; Li, X.; Xu, P. A strategy toward air-stable and high-performance ZnO-based perovskite solar cells fabricated under ambient conditions. *Chem. Eng. J.* **2018,** *336*, 732-740.

(2) Zhang, Y.; Liu, X.; Li, P.; Duan, Y.; Hu, X.; Li, F.; Song, Y. Dopamine-crosslinked TiO_2/perovskite layer for efficient and photostable perovskite solar cells under full spectral continuous illumination. *Nano Energy* **2019,** *56*, 733-740.

(3) Li, H.; Zhang, R.; Li, Y.; Li, Y.; Liu, H.; Shi, J.; Zhang, H.; Wu, H.; Luo, Y.; Li, D.; Li, Y.; Meng, Q. Graphdiyne-based bulk heterojunction for efficient and moisture-stable planar perovskite solar cells. *Adv. Energy Mater.* **2018,** *8*, 1802012.

(4) Niu, T.; Lu, J.; Tang, M.-C.; Barrit, D.; Smilgies, D.-M.; Yang, Z.; Li, J.; Fan, Y.; Luo, T.; McCulloch, I.; Amassian, A.; Liu, S.; Zhao, K. High performance ambient-air-stable $FAPbI_3$ perovskite solar cells with molecule-passivated Ruddlesden-Popper/3D heterostructured film. *Energ. Environ. Sci.* **2018,** *11*, 3358-3366.

(5) Dong, Q.; Fang, Y.; Shao, Y.; Mulligan, P.; Qiu, J.; Cao, L.; Huang, J. Electron-hole diffusion lengths > 175 mu m in solution-grown CH3NH3PbI3 single crystals. *Science* **2015,** *347*, 967-970.

(6) Yang, L.; Wu, M.; Cai, F.; Wang, P.; Gurney, R. S.; Liu, D.; Xia, J.; Wang, T. Restrained light-soaking and reduced hysteresis in perovskite solar cells employing a helical perylene diimide interfacial layer. *J. Mater. Chem. A* **2018,** *6*, 10379-10387.

(7) Ma, Y.; Zhang, H.; Zhang, Y.; Hu, R.; Iiang, M.; Zhang, R.; Lv, H.; Tian, J.; Chu, L.; Zhang, J.; Xue, Q.; Yip, H.-L.; Xia, R.; Li, X. a.; Huang, W. Enhancing the performance of inverted perovskite solar cells via grain boundary passivation with carbon quantum dots. *ACS Appl. Mater. Inter.* **2019,** *11*, 3044-3052.

(8) Wu, Q.; Zhou, W.; Liu, Q.; Zhou, P.; Chen, T.; Lu, Y.; Qiao, Q.; Yang, S. Solution-processable ionic liquid as an independent or modifying electron transport layer for high-efficiency perovskite solar cells. *ACS Appl. Mater. Inter.* **2016,** *8*, 34464-34473.